Nano Research

Open Access

Research Article

Automation assisted systematic investigation on ZIF photonic crystals: From microscopic mechanism to the detection of organophosphorus compounds

Yumeng Gan[1,§], Hualong Sun[1,§], Peichao Hong[1], Weixin Liang[4]✉, Shuping Li[3]✉, and Changxu Lin[1,2]✉

[1] *Research Institute for Biomimetics and Soft Matter, Fujian Provincial Key Lab for Soft Functional Materials Research, Department of Physics, College of Physical Science and Technology, Xiamen University, Xiamen 361005, China*
[2] *State Key Laboratory of Physical Chemistry of Solid Surface, Xiamen 361005, China*
[3] *Fujian Provincial Key Laboratory of Semiconductors and Applications, Collaborative Innovation Center for Optoelectronic Semiconductors and Efficient Devices, Department of Physics, Xiamen University, Xiamen 361005, China*
[4] *Guangdong Provincial Public Laboratory of Analysis and Testing Technology, China National Analytical Center (Guangzhou), Guangzhou 510070, China*
§ *Yumeng Gan and Hualong Sun contributed equally to this work.*

Cite this article: *Nano Research*, **2026**, *19*, 94908381. https://doi.org/10.26599/NR.2026.94908381

ABSTRACT: Metal-organic framework materials exhibit significant advantages in the field of harmful gas adsorption by virtue of their large pore size and high specific surface area. The construction of photonic crystals using zeolitic imidazolate framework-8 (ZIF-8) particles as assembly units can enhance the signal transduction ability, and their polyhedral morphology further expands the ordered arrangement of photonic crystals. In this study, we focus on the optimization of the assembly conditions, response properties, and mechanism of action of ZIF-8 particles, and combine with an automated photonic crystal preparation platform to realize the rapid screening of assembly parameters. The optimized ZIF-8 photonic crystal arrays exhibit selective naked-eye recognition of organophosphorus compounds: It is experimentally confirmed that organophosphorus compounds induce particle size changes through adsorption–surface interactions, which in turn modulate the photonic bandgap widths and lead to the quenching or enhancement of reflectance spectra at specific wavelengths, whereas small-molecule alcohols trigger the spectral quenching of only a single wavelength due to the adsorption-induced particle swelling. The Python-based automated control platform further enables scalable morphology tuning and successfully prepares colored microspheres with tunable photonic properties. This study reveals the ligand-mediated assembly mechanism of metal-organic framework photonic crystals and provides a theoretical basis for the design of metal-organic framework photonic crystals.

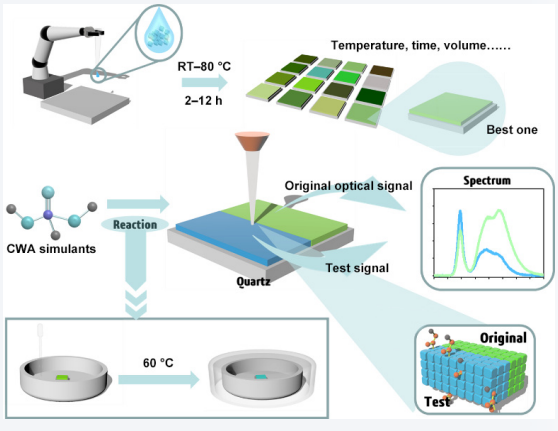

KEYWORDS: metal-organic framework (MOF), photonic crystal, organophosphorus compounds, experiment automation, colloid assembly

1 Introduction

Photonic crystals (PCs), as photonic nanomaterials composed of periodically modulated dielectric materials, have unique photonic band gap (PBG) characteristics. When the PBG falls within the visible light range, PCs can exhibit vivid structural colors by prohibiting the propagation of specific wavelengths of light within this PBG range [1–3]. Historically, photonic crystal sensors developed through particle assembly utilized the response material modulation to controllably tune their optical properties [4–6]. Metal organic framework (MOF) materials have the characteristics of large surface area, high porosity, and diverse structures. When combined with photonic crystal sensors, the composite material can have the characteristics of both PCs and MOFs. For a long time, the

Received: July 7, 2025; **Revised:** December 28, 2025
Accepted: December 29, 2025

✉Address correspondence to Weixin Liang, lweixin920@126.com; Shuping Li, lsp@xmu.edu.cn; Changxu Lin, lincx@xmu.edu.cn

assembly of spherical particles has been a foundational approach for constructing PCs. By assembling crystalline materials into PC structures and making full use of the morphological diversity of particles, PCs can be endowed with richer and more unique optical properties [7–9], which greatly expands the potential of PCs to be used in many fields such as optical sensing, optical communications, and display technologies.

Organophosphorus compounds (OPs) are widely used in agricultural production and as flame retardants, and have a wide range of impacts on daily life, with some of these compounds classified as chemical weapon analogs (CWAs). Their molecular structures closely resemble those of typical chemical warfare agents such as sarin, soman, and VX. For the detection of these substances, the conventional techniques are mainly liquid chromatography (LC), gas chromatography (GC), thin-layer chromatography (TLC), and gas chromatography-mass spectrometry (GC/MS) [10] techniques, which are not suitable for fast detection on site.

Studies showed that MOFs have good adsorption and degradation capabilities for OPs such as methyl paraoxon (MP), methylphosphonic acid (MPA), and dimethyl methylphosphonate (DMMP), while also functioning as high-efficiency filtration media for these hazardous substances in environmental or defense applications [11–16]. The degradation of OPs can be effectively catalyzed by constructing nanoreactors that utilize multi-enzyme synergistic or metalloenzyme synergistic mechanisms [13, 17–19]. In addition, the detection performance of metal-organic framework sensors was significantly improved through metal doping or structural modification [18, 20]. Given the unique performance advantages of polyhedral MOF particles, more and more researchers have chosen them as the assembly matrix for photonic crystal sensors to construct metal organic framework organophosphorus compounds (MOF-PCs) [21–29], which provides new possibilities for combining the advantages of PCs and MOFs for substance detection and sensing, as exemplified by the detection of OPs. In existing studies, some researchers have constructed self-assembled PC using zeolitic imidazolate framework-8 (ZIF-8) particles as a substrate and applied them to the field of gas sensing for the DMMP [30]. However, these works lacked comprehensive exploration of the assembly conditions of MOF-PCs and the sensing principle based on MOF-OPs interactions in terms of microscopic aspects.

In this study, we connect the work pipeline of MOF-PCs including preparation, characterization, and detection systematically (Fig. 1). We achieved a more rational understanding of the colloidal and interface chemistry of MOF PC from combinatorial study of their assembly and interaction with OPs. ZIF-8 PC sensors with good performance and good response to OPs have been prepared, and the exploration of their assembly conditions and the development and expansion of their multidisciplinary applications have been fully completed with the help of an automated PC synthesis platform. Experimental validation showed that the obtained photonic crystal sensors exhibited specific selectivity for OPs. A naked-eye response is first reported for MOF-PCs detecting OPs, bringing in more rapidness and convenience compared with conventional means. In order to further optimize the performance and application qualification of the sensor, we used the automated equipment set to rapidly screen and prepare the MOF-PCs under varied experimental conditions. From the standardized automation data, the mechanism of the superstructure is investigated to help with the deeper understanding of the system, and therefore establishing a new general research paradigm for MOF-PCs.

2 Experimental

Materials: All the chemicals were commercially available.

Synthesis of ZIF-8 particles: First, 1117 mg of dimethylimidazole and 1.3 mg of hexadecyl trimethyl ammonium bromide (CTAB) were dissolved in 5 mL of H_2O as solution A. Then 300 mg of Zn $(CH_3COO)_2{\cdot}2H_2O$ was dissolved in 5 mL of H_2O as solution B. After sonication for 10 min, the two solutions were fully mixed in a 50 mL beaker. Next, solution B was added to solution A at a uniform rate and stirred slowly until the solution turned white. The mixture was kept at 40 °C for 2 h. After centrifugation for 5 min, the product was washed twice with deionized water to obtain ZIF-8 particles.

Configure different concentrations of ZIF-8 colloidal solutions for storage: Colloidal solutions were prepared with product particles at concentrations of 10, 20, and 100 mg/mL.

Self-assembly of MOF crystals: Glass slides were treated with acetone, ethanol, and deionized water for 10 min. After the processed glass slides were dried, the slides were hydrophilically treated using a plasma cleaning machine. 50 μL of colloidal solution was moved onto the glass sheet and the glass sheet was placed in a preheated oven at 60 °C for 2 h.

Automated Synthesis of PC: A colloidal solution with a concentration of 100 mg/mL was selected, and different dosages and assembly temperatures were set in the control program of the automated synthesis platform to quickly assemble the PCs and screen the optimal conditions. The composition of the PC automated synthesis platform and the roles played by each part of the components in the PC synthesis process are shown in Table 1. The speed of the robotic arm was varied according to the detail function stage. Due to the complexity of the automated workflow for photonic crystal microsphere synthesis, detailed control scripts and source codes are being systematically organized and will be disclosed upon final submission.

Characterization: X-ray diffraction (XRD) patterns were obtained using Rigaku IV XRD (CuKα radiation, λ = 1.5406 Å). Scanning electron microscopy (SEM) images were taken using a Carl Zeiss. Nitrogen adsorption isotherms of ZIF-8 samples were measured with a Brunauer–Emmett–Teller (BET).

3 Results and discussion

3.1 Synthesis of ZIF-8 particles

The superstructure assembly of three-dimensional long-range-ordered PCs is usually significantly correlated with the monodispersity, size, and morphology of the functional building

Table 1 Components and functions of the automated preparation platform for PCs

Components	Basic functions	Contribution
Robot arm	Gripping and clamping	Precise transfer of carrier platforms
Syringe pump	Liquid addition	Precise addition of dispersion
Heating platform	Constructing controlled thermal fields	Temperature control

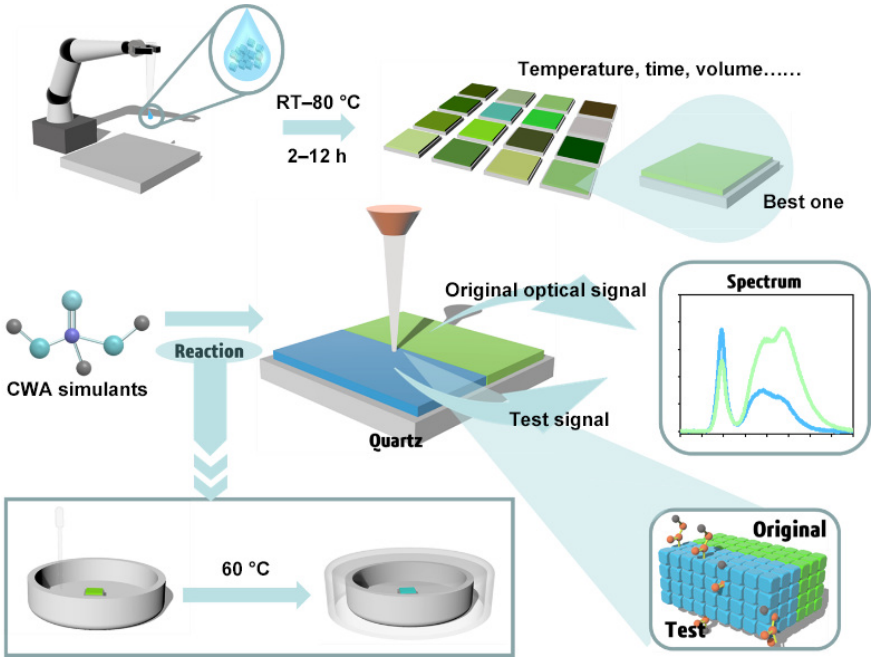

Figure 1 Schematic diagram of the preparation process and sensing principle of photonic crystal sensors.

blocks. Therefore, ZIF-8 particles with different morphologies were synthesized and utilized for superstructure assembly attempts. Among the various shapes of ZIF-8 particles, the cube-shaped particles were selected as the functional building blocks of PCs due to their excellent optical properties and unique naked-eye recognizability.

The structural and physicochemical properties of cubic ZIF-8 particles prepared by the synergistic modulation of CTAB, 2-methylimidazole, and Zn(II) ions were systematically characterized. The XRD signals of the synthesized ZIF-8 particles, subjected to basic characterization and dimensional testing (as shown in Fig. 2(d)), showed peak shapes highly consistent with the simulation results. Figure 2(c) shows the specific surface area of the prepared pristine particles, with an experimental value of 1235 m^2/g, in agreement with literature-reported ZIF-8 specific surface area values. These results indicate the successful synthesis of ZIF-8 particles with good crystallinity. The prepared ZIF-8 particles exhibit good monodispersity, with particle size distribution characterized by narrow dispersion (mainly concentrated at 200 ± 5 nm, as shown in Fig. 2(b)). Particles of this size display bright luster after centrifugation (Fig. 2(a)), which can serve as a macroscopic indicator for rapid quality assessment. SEM morphology analysis (Fig. 2(a)) confirmed that the crystals exhibit a typical truncated rhombic dodecahedron structure.

3.2 Self-assembly of MOF crystals

On the macroscopic scale, the spatial dimension of the assembled PC can reach the centimeter scale, and this property is correlated with the assembly process parameters. To more efficiently investigate the effects of colloidal solution amount and assembly temperature on the assembly effect, PCs with different process parameters were rapidly prepared using an automated PC synthesis platform (Table S1 in the Electronic Supplementary Material (ESM)). This method not only improves the experimental efficiency, but also systematically optimizes the conditions to obtain the best assembly effect quickly.

The reflectance spectral signals were combined with optical microscopy pictures, and the ZIF-8 PCs with high-quality were screened out. The experimental results show that the PCs under certain assembly conditions exhibit a coffee ring effect under the combined effect of different temperatures, particle concentrations, and surfactants. All reflectance spectra shown in Fig. 3 were obtained from five independent repeated experiments (n = 5). The spectral deviations observed in certain units correspond to non-optimal assembly parameters and were intentionally retained for parameter screening, rather than indicating intrinsic instability of the photonic crystal system.

Under low-temperature assembly conditions, the evaporation rate of the colloidal solution is slow, the thermal motion of the particles is less intense, and inter-particle interactions dominate the assembly process. This results in a large number of particles accumulating in the central region with an inconspicuous outer ring (Fig. S7 in the ESM). When the temperature is elevated, the dispersion exhibits a rapid evaporation rate with intensified droplet evaporation effects. Under these conditions, the particle thermal motion becomes more vigorous, and the influence of particle concentration on assembly becomes predominant. At low particle concentrations, strong edge evaporation induces capillary flow that transports particles to the droplet periphery, thereby forming distinct coffee ring patterns. Conversely, at high particle concentrations, enhanced thermal motion combined with surfactant effects significantly increases interparticle contact probability. This promotes the formation of large, stabilized aggregates that resist capillary flow, unlike individual particles, thus effectively suppressing coffee ring formation (Fig. S7 in the ESM).

At moderate temperatures, assembly is affected by a variety of factors. When the number of particles is large, on the one hand, the thermal movement of particles is not as intense as at high temperatures, and the aggregates are not fully stabilized, which counteracts the influence of capillary flow; on the other hand, due to the large number of particles, the liquid is affected by the surface tension at the edges, and the two aspects work together to form an

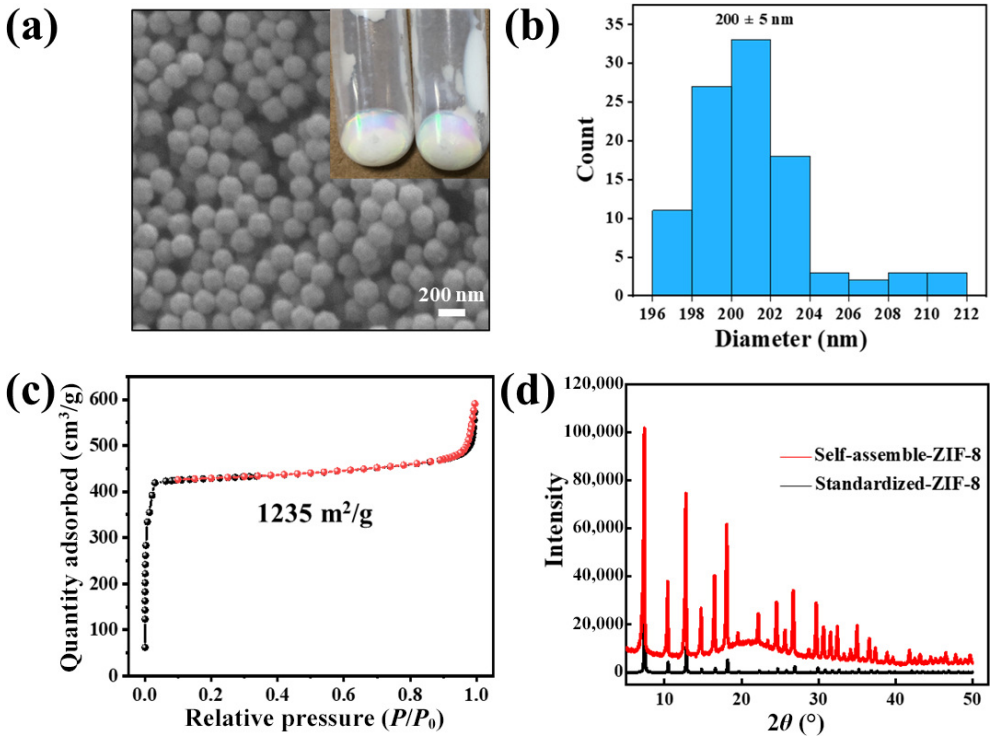

Figure 2 The basic physical properties of ZIF-8 particles. (a) The SEM image of the particles. (b) The particle size distribution, reflecting the distribution characteristics of particle diameters. (c) The adsorption–desorption curve of the particles. (d) The XRD patterns of the particles and the comparison diagram with the simulated signal.

obvious coffee ring (Figs. S7 and S8 in the ESM). When the amounts of particles are small (80 μL), a slight outer ring reappears due to the hydrophilicity of the substrate and the effect of edge tension, resulting in a partly dense and partly loose microstructure (Figs. S7 and S8 in the ESM).

In the variation of assembly volume, the G channel values are higher at 80, 100, and 120 μL under different assembly temperatures; temperature has a more direct effect on the assembly quality of PCs, with the red, green, and blue (RGB) channel pixel values generally increasing with temperature (Fig. S9 in the ESM).

After several screenings, the ideal coverage effect was found to be achievable by using 100 μL of colloidal solution with a concentration of 100 mg/mL, which was just enough to uniformly cover the surface of a 10 mm × 10 mm quartz substrate, thereby avoiding assembly defects caused by insufficient or excessive solution.

3.3 Response of self-assembled ZIF PC to OPs

Three OPs, MP, MPA, and DMMP, were selected in this study, while common alcohol solvents were chosen as the analyte control group. The assembled photonic crystal sensors were reacted by direct exposure to the atmospheres of DMMP, MP, and MPA. The spectral analysis (Fig. 4) shows an excellent agreement between the reflectance spectra of different microregions of the same PCs. The initial sample shows two groups of reflection peak: the 450 and 500–600 nm bands. With the comparison over the reflectance of bare glass substrate, 450 nm was the background peak of the experimental setup. However, the 450 nm peak of the bare glass substrate was very weak from the signal/noise ratio aspect (Fig. S22 in the ESM). The intensity of 450 nm peak could be used as the indicator of the surface smoothness and degree of order of ZIF assemblies (Fig. 3) due to the diffuse reflection. For the optimized photonic crystal sensors shown in Fig. 4, repeated measurements (n = 5) exhibit nearly fully overlapped reflectance spectra, demonstrating excellent optical response stability and reproducibility under identical sensing conditions.

When exposed to DMMP atmosphere, the intensity of the characteristic peak at 450 nm is attenuated by about 41.82%, whereas the reflected intensity in the 500–600 nm band increases to 2.34 times the original intensity, and there is a displacement of the high peak from 500 to 600 nm. The reaction with MPA was similar to that of DMMP, with a significant increase in the reflectance intensity in the 500–600 nm band and the same displacement of the high peaks. Comparison experiments show that exposure to MPA leads to a similar attenuation of the intensity in the 450 nm band (~ 42.8%), and the reflectance intensity in the 500–600 nm region is increased to 1.78 times of the original one, with an increase in the amplitude of the bimodal region by $\Delta\lambda$ = 1.3 nm, and a red shift of the higher peaks by $\Delta\lambda$ = 48.01 nm. Unlike DMMP and MPA, the reflectance spectra of PC reacting with MP did not show obvious attenuation or enhancement of light intensity.

It is worth noting that alcohols show a different reaction mechanism from that of OPs in the reflectance spectra. The intensities in the 450 nm band are significantly reduced by about 60.8% with methanol and 56.4% with ethanol. Although there is no significant change in the intensity in the 500–600 nm region, the distribution of the high peaks becomes haphazard, and homogeneity is significantly reduced. SEM characterization (Fig. 5) shows that ethanol molecules cause swelling of ZIF-8 particles, while local agglomeration leads to a widening of the particle spacing distribution, which disrupts the long-range ordering of the PCs. This inhomogeneous structural distortion plausibly explains the wavelength fluctuations of the high peaks observed in the reflectance spectra.

We speculate that the different effects of alcohol molecules and OPs molecules on ZIF-8 PCs may stem from the synergistic effects

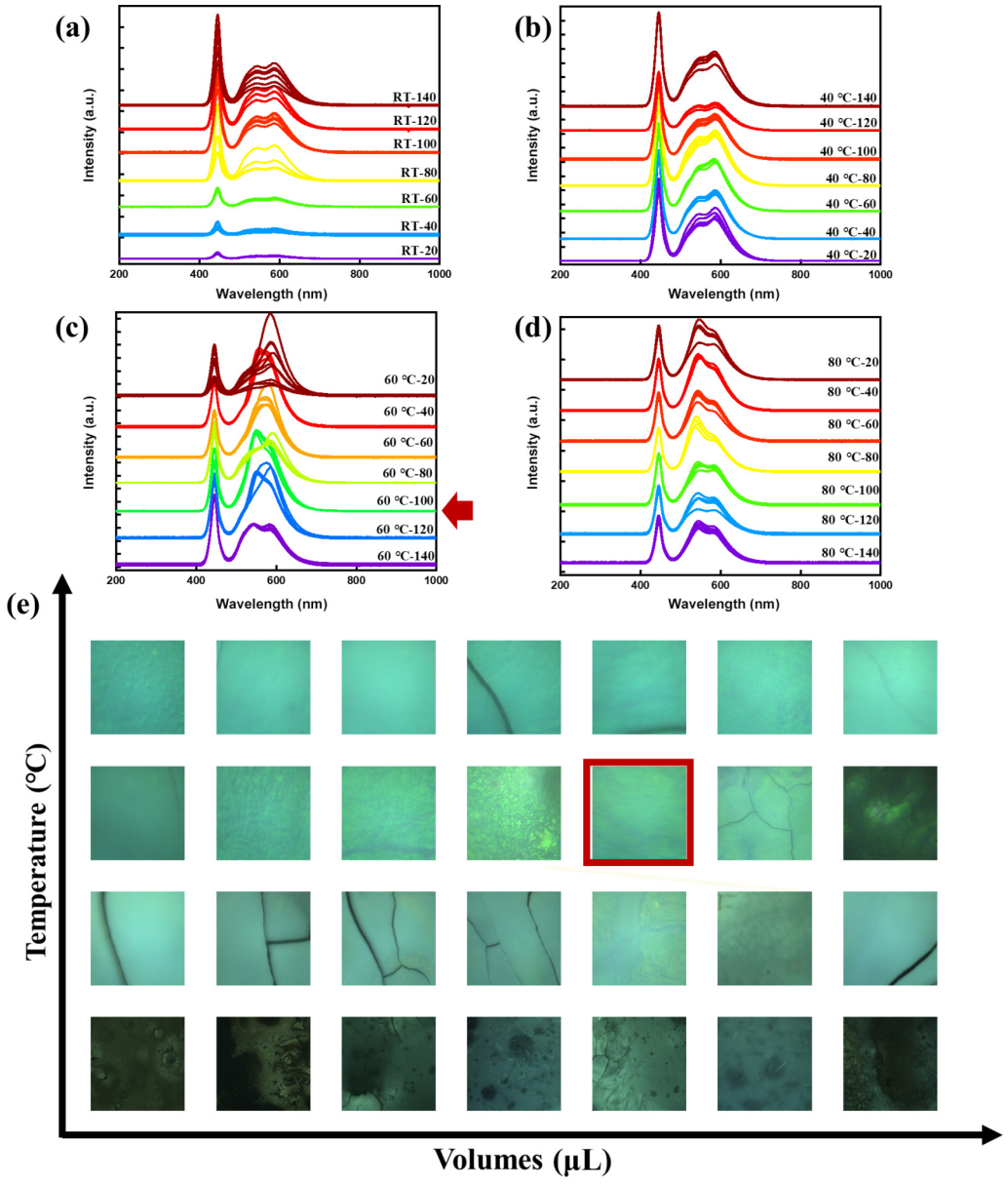

Figure 3 Automated platform for rapid screening of PC preparation conditions. (a)–(d) Spectra of PC assembled at the same temperature with different particle additions. (e) Optical images of PC corresponding to the dual dimensions of temperature and particle additions (red boxes are the best).

of size and polarity. Small-sized alcohol molecules enter the ZIF-8 pores and initiate dynamic pore contraction through hydrogen bonding, weakening the peak intensity at 450 nm but failing to initiate lattice expansion, leaving the peak at 500–600 nm unchanged. DMMP/MPA with strong polar groups preferentially interact with the surface, leading to local structural collapse. They may trigger solvation swelling or molecular layer coverage on the surface, leading to the displacement of the reflection peaks at high peaks. On the other hand, MP has no significant spectral response due to its large size and too strongly polarized phosphonate group. The rigid structure of MP makes it unable to cause deformation of the ZIF-8 lattice, so its spectral change is negligible.

The experimental results show that when the PCs were exposed to DMMP and MPA atmospheres, the structural colors observable by naked-eye disappeared (Fig. 6), whereas in the MP atmosphere, the structural colors of the PCs remained basically unchanged. For further comparative analysis, this study conducted control experiments with ethanol and methanol under the same conditions. The results demonstrate that the system exhibits an extinction phenomenon distinct from that of OPs. From the optical images, the slight differences in structural colors of the PCs exposed to alcohols and OPs can be clearly distinguished, indicating that the PCs formed by self-assembly of ZIF-8 particles are selective in response to OP molecules.

Optical microscopy analysis reveals that both alcohol interfering agents and OPs exhibit similar warm-yellow hues post reaction. This chromatic overlap, combined with the limited resolution of human vision, can result in misinterpretation during naked-eye observation. To address this, RGB channel peak shifts in optical images were analyzed (Fig. 6). RGB values were extracted from optical images using a Python-based image processing script. For each sample, at least three independent measurements (n = 3) were analyzed. RGB intensities were normalized to the maximum channel value of the original photonic crystal to minimize

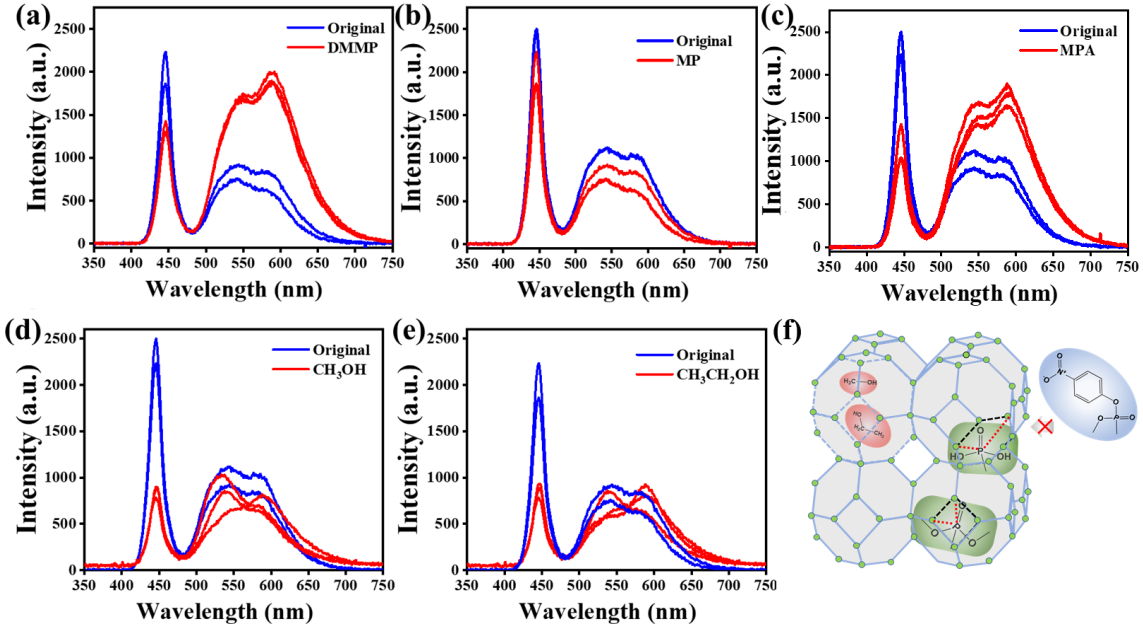

Figure 4 Reflectance spectra of PCs in their original state, and comparison of reflectance spectra after reaction with OPs and with alcohols in the control group. (a) Reflectance spectra of assembled PCs after complete reaction with DMMP to saturation. (b) Reflectance spectra of assembled PCs after complete reaction with MP to saturation. (c) Reflectance spectra of assembled PCs after complete reaction with MPA to saturation. (d) Reflectance spectra of PCs after complete reaction with methanol (control) to saturation. (e) Reflectance spectra of PCs after complete reaction with ethanol (control) to saturation. (f) Principle of spectral response generation by PCs.

illumination-induced variations. The results are presented as mean values with standard deviation. The G > R and B > R sequences were demonstrated to remain unchanged after MP exposure, corresponding to stable structural colors. Alcohol exposure was found to induce the most pronounced increase in the R-channel intensity, resulting in GRB ordering, which aligns with the red shift phenomenon caused by solvent-induced structural disorder. In contrast, OPs significantly reduced B channel intensity, with DMMP showing a marked expansion in the B/G differential, forming a distinct fingerprint pattern (R > G >> B). Based on these findings, the ZIF-8-based photonic crystal sensor establishes a tri-mode detection system: structural color screening, RGB ratio validation, and PCA-assisted classification (Fig. S18 in the ESM). This system enables rapid *in situ* detection by replacing complex chromatographic analyses with optical signals while minimizing false-positive rates.

Although the sensor selectively discriminates alcohols from OPs, its ability to differentiate structurally analogous OPs remains limited. The principal component analysis (Fig. S18 in the ESM) effectively distinguishes alcohol and OP signals but exhibits reduced discriminative power among structurally similar OPs. Although the algorithm is compatible with lightweight computing architectures, its efficacy in resolving subtle selectivity variations requires further optimization through synergistic enhancement strategies. These results highlight the sensor's robust selectivity between OPs and alcohols, whereas precise identification of analogous OPs necessitates multidimensional signal integration techniques. Although the current ZIF-8 photonic crystal sensor shows limited discrimination between structurally similar OPs such as DMMP and MPA, selectivity may be further improved through several strategies. These include regulating the ZIF framework structure or particle size distribution, introducing surface functionalization to create differentiated host–guest interactions, and integrating multidimensional optical signals such as reflectance peak position, bandwidth, and RGB evolution.

3.4 Response mechanism of ZIF photonic crystal sensor formed by self-assembly

PCs exhibit bright structural colors that originate from the ordered arrangement of matrix particles, and this periodic structure in turn forms the PBG. To investigate the effect of periodic structure changes on the response to OPs, the self-assembled structures before and after the reaction were characterized by SEM in this study. As shown in Fig. 5(a), the self-assembled ZIF-8 particles exhibit an ordered arrangement.

As shown in Fig. 5(b), after exposure to a DMMP atmosphere, the structural adhesion between ZIF-8 particles occurs alongside a reduction in particle size. In an MPA atmosphere, the particle size variation and interparticle adhesion are observed, with adhered particles forming a lamellar structure. In an MP atmosphere, despite significant particle size alteration, the particles adopt a denser arrangement, thereby partially retaining the original optical structure.

Figures 5(e) and 5(f) demonstrate that after exposure to methanol and ethanol atmospheres, the particles undergo significant size expansion, with their assembled structures exhibiting pronounced irregularities. The increased particle size alters the PBG, causing a red shift in the reflected wavelength. When the wavelength exceeds the visible spectrum range, no distinct structural color is detectable by naked-eye observation.

These results demonstrate that the self-assembled ZIF-8-based PC structures can serve as sensing materials for OP differentiation and detection. The optical property changes of PCs primarily originate from PBG modulation. The selectivity between OPs and alcohols is attributed to their differential effects on the PC structures. Specifically, non-periodic structures formed by particles through interparticle adhesive interactions modify light propagation paths within the crystal, thereby altering photon transport modes and ultimately inducing significant optical property changes. According to the Bragg–Snell relationship, the photonic band gap

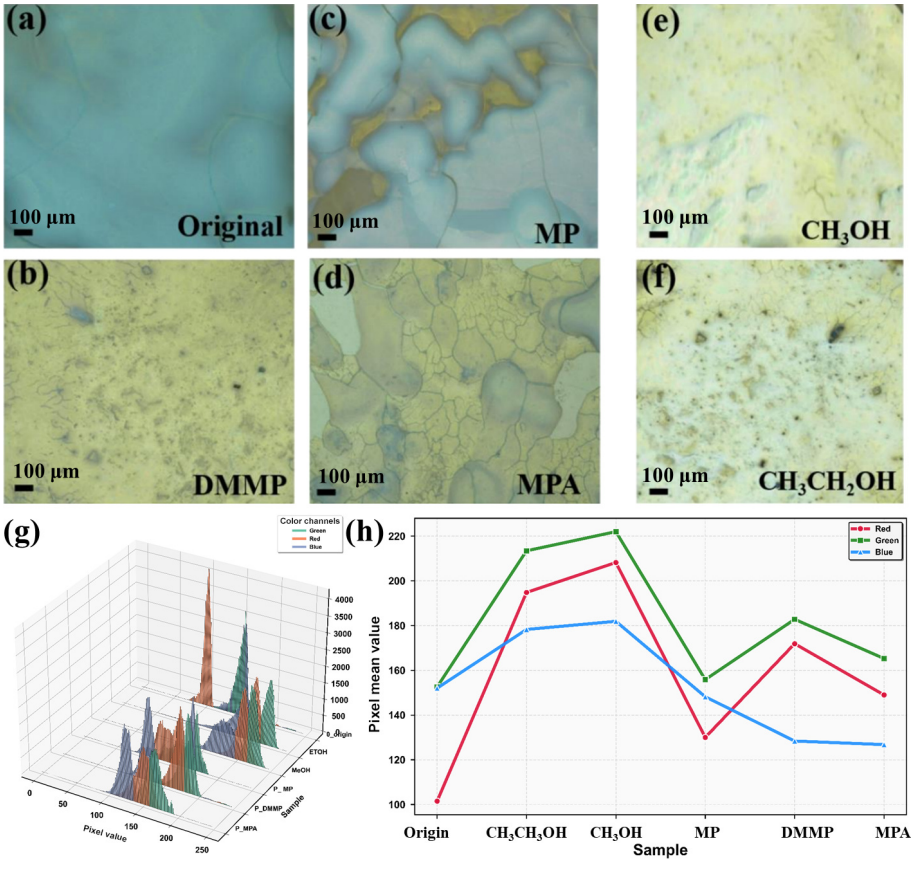

Figure 5 Optical images of the PCs in the original state, and the comparison of optical images after reaction with OPs and with the control group of alcohol substances. (a) The optical image of the assembled PCs in the original state. (b) The optical image of the assembled PCs after saturation reaction with DMMP. (c) The optical image of the assembled PCs after saturation reaction with MP. (d) The optical image of the assembled PCs after saturation reaction with MPA. (e) and (f) The optical images of the PCs after saturation reactions with the alcohol control substances, respectively. (g) Distribution diagrams of RGB values and peak pixel values of three channels for optical images of different reactants. (h) Each RGB data point represents the statistically processed result obtained from three independent measurements (n = 3).

position is proportional to the effective lattice spacing and refractive index. Therefore, the adsorption-induced particle shrinkage or swelling leads to corresponding blue or red shifts of the PBG. Due to the structural disorder and local heterogeneity, an exact linear relationship is difficult to establish; however, a clear monotonic correlation between particle size variation and PBG shift is consistently observed.

Figure 7 further illustrates the synergistic mechanism of adsorption between different molecules and ZIF-8 photonic crystals. With the help of structural models (Figs. 7(a)–7(e)), it can be seen that the small-sized alcohols can enter the ZIF-8 pores smoothly due to their small molecular dynamics diameter. After entering the pore, the interaction between the alcohol molecules and ZIF-8 results in the shrinkage of the pore, which leads to the localized deformation of the material, and ultimately results in the attenuation of the 450 nm reflection peaks. In contrast, the adsorption capacity of DMMP and MPA is weaker than that of small-sized alcohols, but the adsorption phenomenon still exists. This explains the burst and enhancement of DMMP and MPA at specific wavelengths of the reflectance spectrum: On the one hand, their adsorption causes local deformation of the material, resulting in the attenuation of the 450 nm peaks; on the other hand, the strong polar phosphoric acid groups contained in DMMP and MPA may interact with the surface structure of ZIF-8, which may lead to the collapse of the structure of ZIF-8 through the solvation effect or molecular coverage effect, and ultimately to the collapse of the structure at 500 nm. On the other hand, the strong polar phosphate groups in DMMP and MPA may interact with the surface structure of ZIF-8 and cause structural changes of ZIF-8 through solvation or molecular coverage effects, resulting in the formation of enhanced reflection peaks in the 500–600 nm region. It is noteworthy that the MP molecules with benzene ring structure do not penetrate the ZIF-8 pores and match the lattice effectively due to their large spatial resistances and weak polarity, so the spectral responses do not show significant changes (Fig. 4(b)).

To deeply investigate the sensor's response mechanism to OPs, this study selected DMMP as a representative analyte. When the PCs saturate in high-concentration DMMP environments, dendritic patterns become distinctly visible in optical micrographs. As shown in Fig. S22(c) in the ESM, these characteristic growth patterns correlate with DMMP diffusion through ZIF-8 pores. The adsorbed saturated particles resemble crystalline seeds that diffuse outward with increasing DMMP concentration while undergoing agglomeration, a process analogous to dendritic growth.

In contrast, the alcohol diffusion in ZIF-8 particles exhibits island-like characteristics, with aggregated particles forming layered structures that display partial cementation and dispersion (Fig. S22(e) in the ESM). Notably, neither diffusion–agglomeration mode alters ZIF-8 crystallinity but modulates optical signals through ordered structural adhesion and collapse (Fig. S22(a) in the ESM).

Under DMMP concentration changes, reflectance spectral

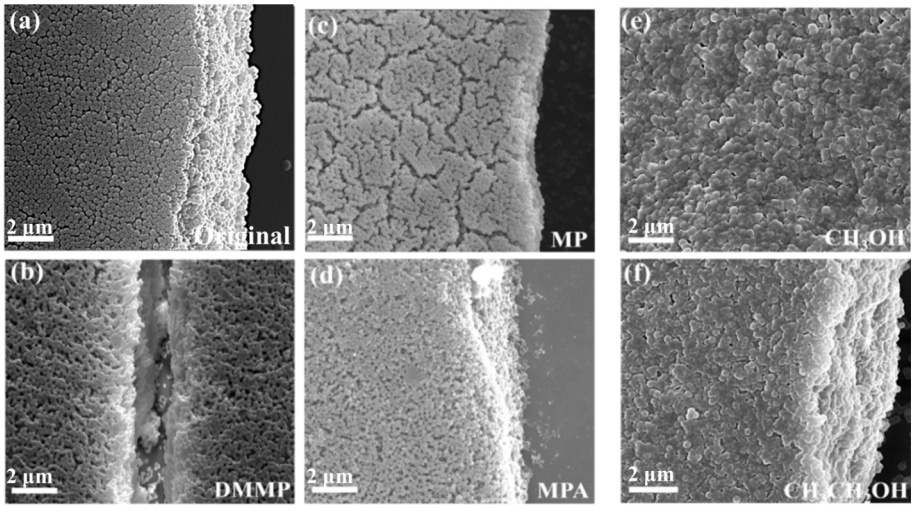

Figure 6 SEM images of the PCs in the original state, and the comparison diagrams of the optical images after the reaction with OPs and after the reaction with the alcohol substances in the control group. (a) The SEM image of the assembled PCs in the original state. (b) The SEM image of the assembled PCs after a saturation reaction with DMMP. (c) The SEM image of the assembled PCs after a saturation reaction with MP. (d) The SEM image of the assembled PCs after a saturation reaction with MPA. (e) and (f) The SEM images of the PCs after saturation reactions with the alcohol control substances, respectively.

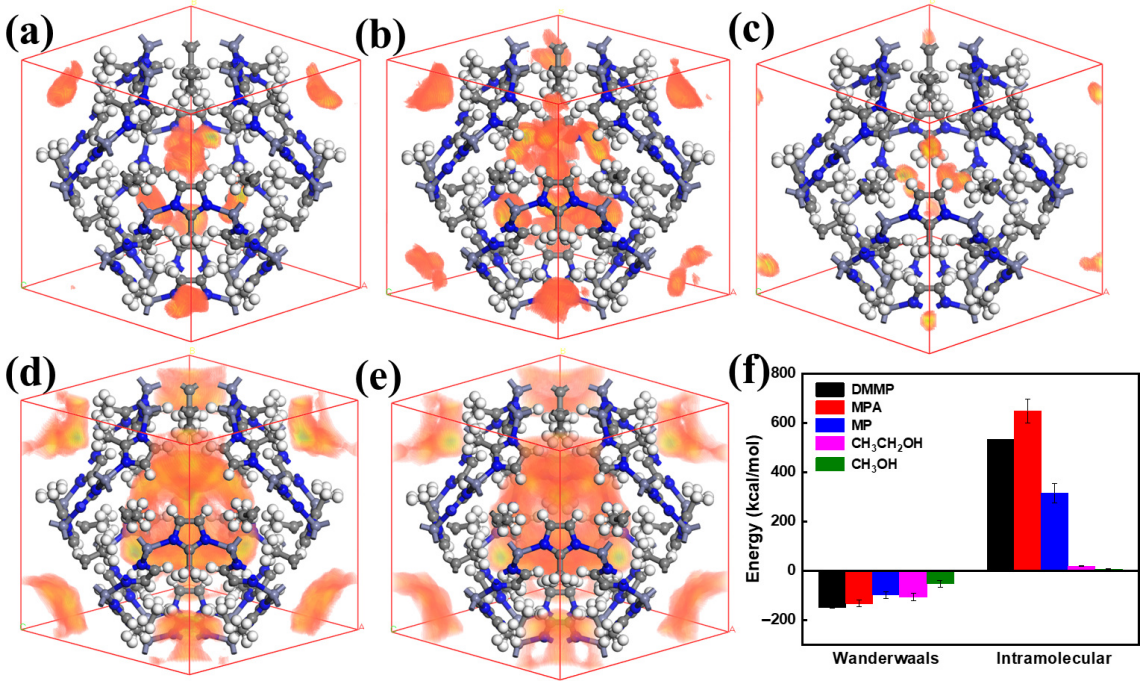

Figure 7 Adsorption of ZIF-8 particles for different gases at 60 °C simulated using Material studio software. (a)–(e) Corresponding to the adsorption of DMMP, MPA, MP, CH_3CH_2OH, and CH_3OH, respectively. (f) The energy distribution in the adsorption.

signals diminish progressively until stabilizing in a non-reflective state (Fig. S16 in the ESM). At DMMP saturation, the particle pore size remained unchanged (~ 1.5 nm), whereas the specific surface area decreased from 1235 to 7 m^2/g, and the adsorption isotherm transitioned from type I(b) to type III. This suggests that the DMMP in the ZIF-8 pores is saturated and the ZIF-8 voids have weakened nitrogen interaction forces, as evidenced by reduced adsorption at saturation pressure (Fig. 8).

For the DMMP adsorption and diffusion in ZIF-8, further analysis was conducted by nuclear magnetic resonance (NMR) and Fourier transform infrared (FTIR) (Figs. S20 and S21 in the ESM). The adsorption of DMMP molecules in ZIF-8 PC was further confirmed by fingerprinting the characteristic peaks of DMMP in NMR and FTIR. These results suggest that the porosity of ZIF-8 particles plays an important role in the performance of photonic crystal sensors.

By studying the time series of the reaction process of PC with DMMP, it was found that after 10 min of reaction, the particles began to stick together. With time, the adhesion between the particles became more severe, and voids gradually formed. As the voids increased, the ordered structure began to collapse, eventually leading to extinction (Fig. 9(a)). By analyzing the RGB values of the optical image, it was observed that the adhesion between particles significantly affected the pixel values of the G channel. When the voids caused by adhesion expanded to the point where they could not support the periodic structure, the pixel values of the R and B

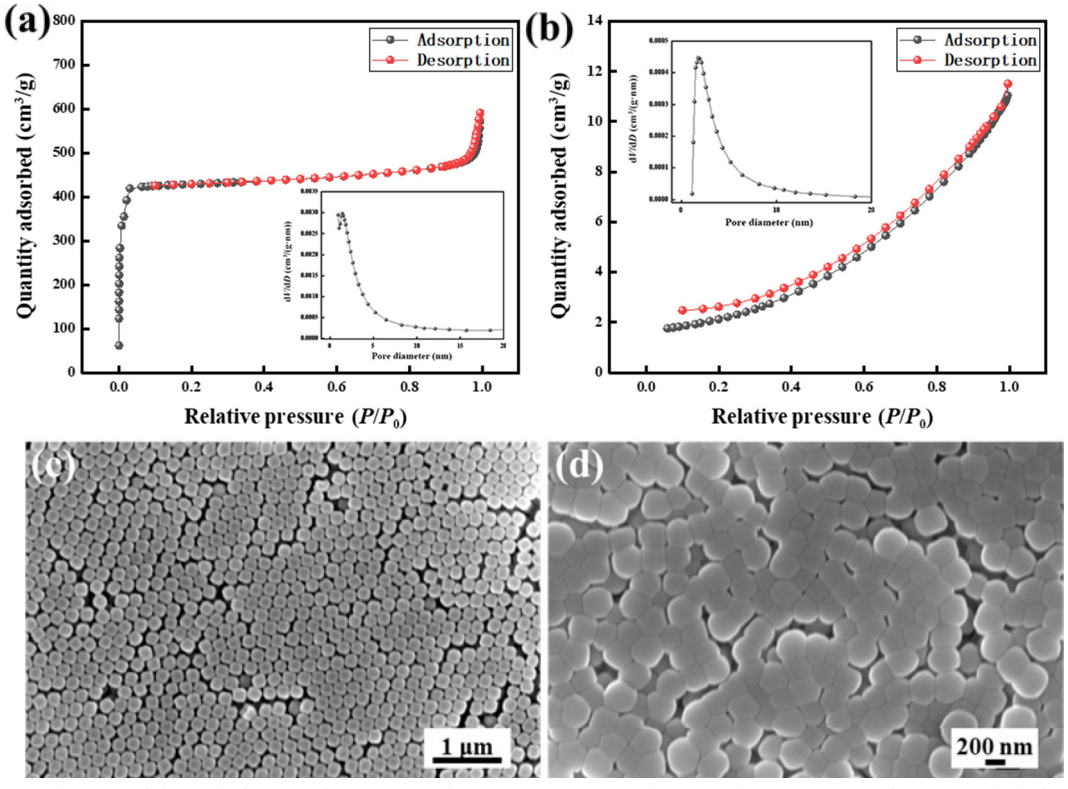

Figure 8 Comparison diagrams of changes before and after reaction with DMMP: (a) nitrogen adsorption–desorption curves of ZIF-8 particles before reaction and (b) adsorption–desorption curves of ZIF-8 particles after reaction with DMMP. (c) Assembly structure of the original PCs. (d) Assembly structure of the PCs after reaction with DMMP.

channels changed significantly, which eventually led to optical extinction (Fig. 9(d)).

In contrast, the reaction process of MPA showed different characteristics: initial aggregation of particles and creation of voids, followed by progressive adhesion of particles over time, eventually leading to structural collapse. This result is similar to that of DMMP reaction but with a distinct reaction pathway (Fig. S17 in the ESM).

3.5 Rapid expansion of self-assembly optimal condition studies using automated equipment and algorithms

Our ZIF-8-based photonic crystal sensor offers distinct advantages over existing systems. Conventional opitcal sensors for OPs often rely on enzymes, which are fragile and limit real-world use. In contrast, our sensor uses ZIF-8 for direct, enzyme-free recognition, ensuring greater robustness.

Furthermore, ~ 3.4 Å of ZIF-8 pore provides exceptional molecular sieving selectivity for small OPs, a key advantage over other MOFs with larger, non-selective pores. The integration of this selective MOF into a photonic crystal enables a direct visual readout, a rare feature in MOF-based sensing. This unique combination of enzyme-free operation, precise size selectivity, and simple visual detection distinguishes our platform and highlights its potential for practical on-site monitoring.

In addition, the assembly of ZIF-8 particles to form PCs was briefly extended using an automated PC synthesis platform, and rapid investigation attempts were made into the effects of different assembly temperatures on PCs. Furthermore, ZIF-8 photonic crystal microspheres were also prepared using the automated platform (Fig. 10).

The automated PC preparation platform is a highly integrated and intelligent system, primarily composed of three core components: a robotic arm, an injection system, and a heating system. During platform operation, the robotic arm simulates human hand movements and flexibly switches between the injection and heating systems. As shown in Fig. 10(a), the robotic arm exhibits high versatility and flexibility, enabling precise clamping of substrates for photonic crystal microsphere or planar PC preparation.

For PC microsphere synthesis, the robotic arm controls the injection system to deliver specific solutions into molds or reaction environments per predefined protocols, while coordinates with the heating system to maintain optimal temperatures. The movement speed of the robotic arm is dynamically adjusted according to the specific task, such as substrate transfer, solution dispensing, or positioning. When the robotic arm carries and supports liquid droplets during colloidal assembly, relatively low speeds are applied, specifically ~ 30 cm/s for dispersion assembly and 50–80 cm/s for movements between different operation stations, in order to ensure uniform droplet spreading and stable evaporation. In contrast, during unloaded motions without droplet support, the robotic arm can operate at higher speeds of 100–300 cm/s to improve overall operational efficiency. This induces solution self-assembly under controlled conditions, forming PC microspheres. For planar PC fabrication, the robotic arm uniformly deposits materials onto planar substrates through precise motions, leveraging heating system temperature control to achieve ordered material arrangement and high-quality planar PCs.

The advantages of platform include not only rapid screening of PC assembly conditions to significantly enhance experimental efficiency and exploration speed but also scalable PC microsphere

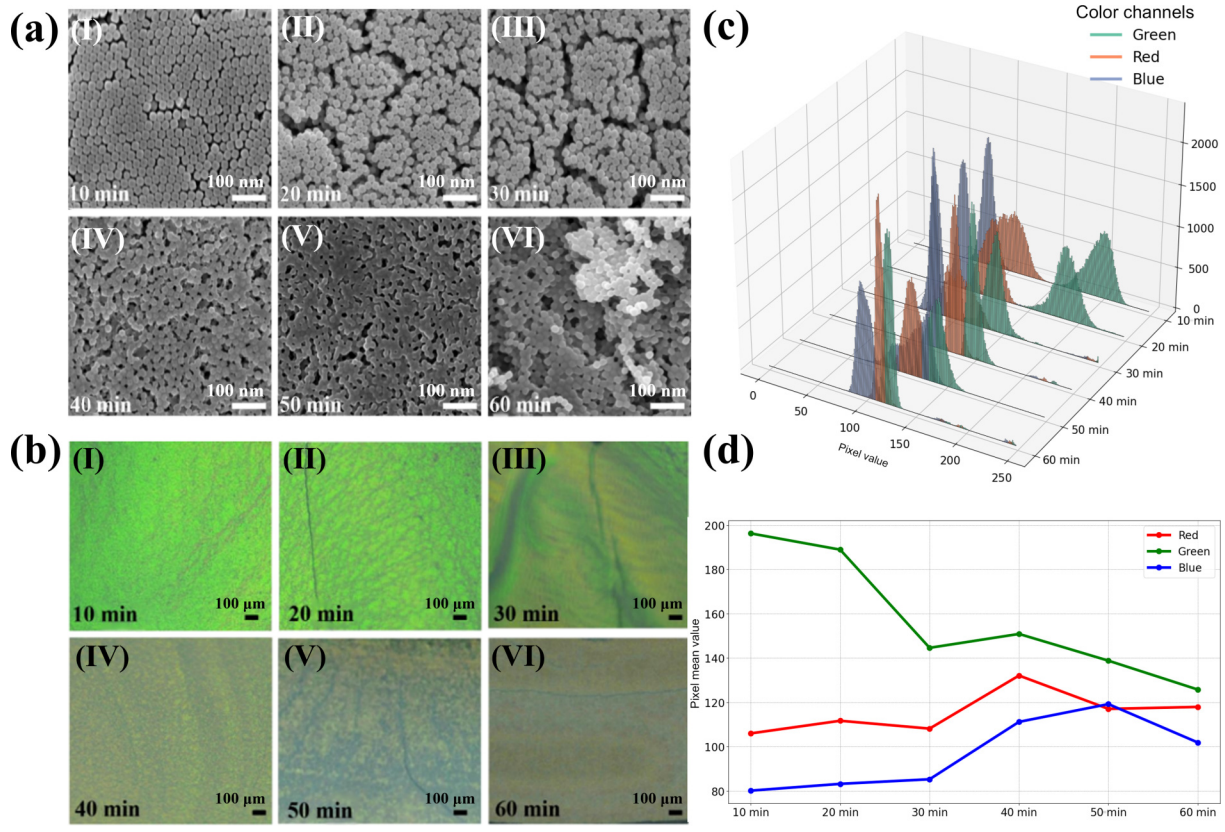

Figure 9 Images of microstructural changes in PC sensors after reaction with DMMP at different time intervals were acquired through multiple characterization techniques. (a) Microstructural evolution of PC sensors after varying reaction times observed via SEM. (b) Structural color variations of PC sensors after different reaction time captured by optical microscopy. (c) Statistical analysis plots of optical images analyzed using the RGB method. (d) Temporal trends of RGB values extracted from optical images at different reaction stages.

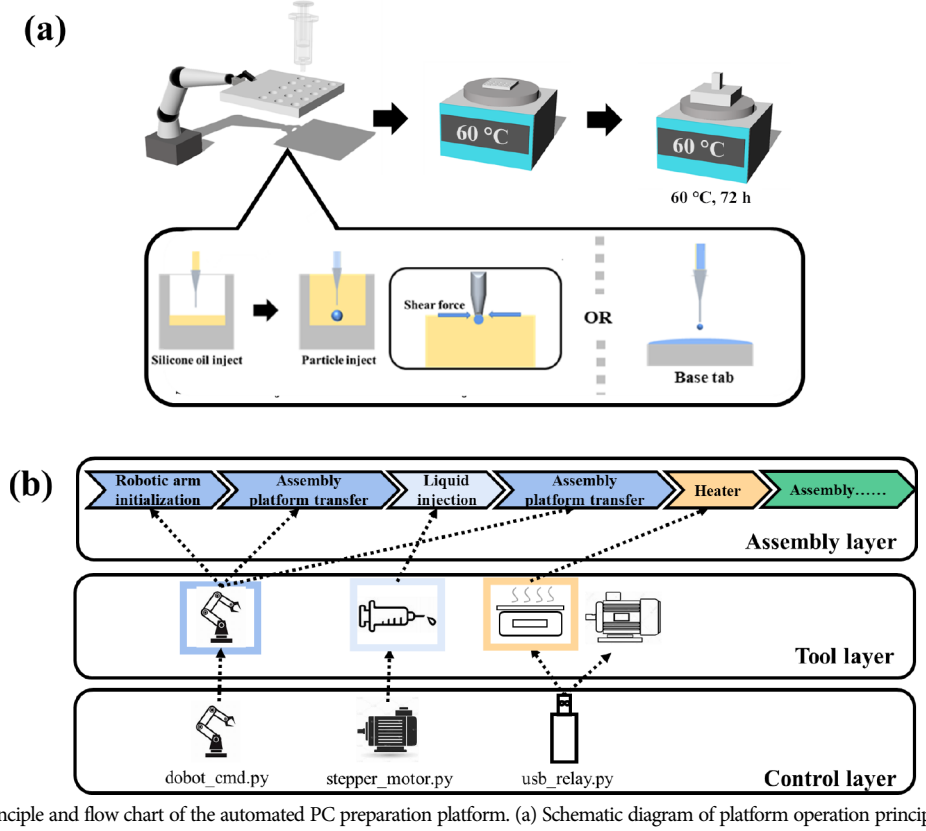

Figure 10 Operation principle and flow chart of the automated PC preparation platform. (a) Schematic diagram of platform operation principle. (b) Schematic diagram of platform control mode and PC preparation flow.

synthesis enabled by innovative substrate replacement and liquid injection methods.

The prepared PC microspheres exhibit structural coloration observable to the naked eye. A dense and uniform arrangement of ZIF-8 particles is visible in SEM imaging after fracturing a section of the microspheres (Fig. 11). The reflectance spectra exhibit dual peaks within the range of 500–600 nm, with the primary peak centered at 600 nm.

4 Conclusions

This study demonstrates the successful assembly of ZIF-8-based MOF-PCs with enhanced optical sensing capabilities for OPs. By optimizing colloidal assembly conditions and leveraging an automated synthesis platform, we achieved rapid parameter screening and scalable fabrication of high-quality MOF-PC arrays. The automated methodology significantly accelerated the exploration of temperature, concentration, and surfactant effects, enabling precise control over particle arrangement and photonic bandgap modulation. The resulting MOF-PCs exhibited selective naked-eye detection of OPs such as DMMP and MPA through adsorption-induced structural changes, while distinguishing them from interfering alcohols via distinct reflectance spectral shifts and RGB channel analysis.

The integration of automation not only streamlined the preparation process but also provided standardized data for mechanistic insights, revealing OPs-specific response mechanisms. The MOF-PCs' ability to translate molecular interactions into visible optical signals highlights their potential for on-site environmental monitoring, chemical threat detection, and portable sensing devices. Furthermore, the automated platform's versatility in synthesizing tunable photonic microspheres underscores its applicability in advanced optical materials design.

This work establishes a paradigm for combining MOF versatility with photonic crystal engineering, emphasizing automation as a critical enabler for reproducibility and scalability. Future efforts will focus on enhancing selectivity for structurally similar OPs and expanding the platform to diverse MOF architectures, paving the way for next-generation smart sensors and multifunctional optical systems.

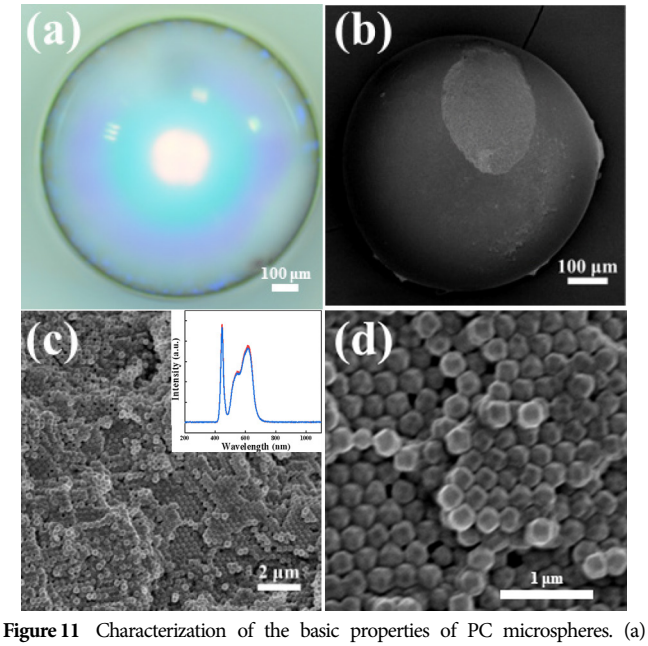

Figure 11 Characterization of the basic properties of PC microspheres. (a) Optical image with corresponding spectrum. (b) Microsphere morphology under SEM. (c) and (d) Microsphere internal assembly morphology under SEM. Inset: the spectrum of PC microspheres.

Electronic Supplementary Material: Supplementary material (the synthesis of ZIF-8 particles, exploration of ZIF-8 particle self-assembly conditions, optical images, spectral data, and physical images) is available in the online version of this article at https://doi.org/10.26599/NR.2026.94908381.

Data availability

All data needed to support the conclusions in the paper are presented in the manuscript and the Electronic Supplementary Material. Additional data related to this paper may be requested from the corresponding author upon request.

Acknowledgements

This research was financially supported by the Fundamental Research Funds for the Central Universities (No. 20720240142), the Higher Education Discipline Innovation Project (No. B16029), Xiamen Natural Science Fund (No. 3502Z202473030), Open Fund of Guangdong Provincial Key Laboratory of Metrology & Testing Technology (No. KF2024002), and GuangDong Basic and Applied Basic Research Foundation (No. 2023A1515011156).

Declaration of competing interest

All the contributing authors report no conflict of interests in this work.

Author contribution statement

Y. M. G.: Investigation, formal analysis, writing – original draft. H. L. S.: Investigation. P. C. H.: Methodology. W. X. L.: Resource, funding acquisition. S. P. L.: Supervision, funding acquisition. C. X. L.: Conceptualization, writing – review & editing, project administration, funding acquisition. All the authors have approved the final manuscript.

Use of AI statement

During the preparation of this work, the authors used Chatgpt in order to screen and correct typo and grammar error. After using this tool/service, the authors reviewed and edited the content as needed and take full responsibility for the content of the publication.

References

[1] Yablonovitch, E.; Gmitter, T. J. Photonic band structure: The face-centered-cubic case. *Phys. Rev. Lett.* **1989**, *63*, 1950–1953.

[2] Yablonovitch, E. Inhibited spontaneous emission in solid-state physics and electronics. *Phys. Rev. Lett.* **1987**, *58*, 2059–2062.

[3] Lin, S. Y.; Fleming, J. G.; Hetherington, D. L.; Smith, B. K.; Biswas, R.; Ho, K. M.; Sigalas, M. M.; Zubrzycki, W.; Kurtz, S. R.; Bur, J. A three-dimensional photonic crystal operating at infrared wavelengths. *Nature* **1998**, *394*, 251–253.

[4] Huang, C. K.; Chan, C. H.; Chen, C. Y.; Tsai, Y. L.; Chen, C. C.; Han, J. L.; Hsieh, K. H. Rapid fabrication of 2D and 3D photonic crystals and their inversed structures. *Nanotechnology* **2007**, *18*, 265305.

[5] Wang, F.; Feng, L.; Qin, Y.; Zhao, T.; Luo, H. J.; Zhu, J. F. Dual functional SiO_2@TiO_2 photonic crystals for dazzling structural colors and enhanced photocatalytic activity. *J. Mater. Chem. C* **2019**, *7*, 11972–11983.
[6] Lu, Y. S.; Vijayakumar, S.; Chaix, A.; Pimentel, B. R.; Bentz, K. C.; Li, S.; Chan, A.; Wahl, C.; Ha, J. S.; Hunka, D. E. et al. Remote detection of HCN, HF, and nerve agent vapors based on self-referencing, dye-impregnated porous silicon photonic crystals. *ACS Sens.* **2021**, *6*, 418–428.
[7] Amrehn, S.; Wu, X.; Wagner, T. Tungsten oxide photonic crystals as optical transducer for gas sensing. *ACS Sens.* **2018**, *3*, 191–199.
[8] Wang, Y. R.; Gao, Y. F.; Wang, Z. L.; Yan, J.; Chen, Y. L. Ultra-trace chlorinated gases optical sensor with moisture-resistant based on structural-customizable UiO-66 3D photonic crystals. *Sens. Actuators B: Chem.* **2023**, *393*, 134219.
[9] Wang, M. Y.; Liu, Y. X.; Sun, Y. T.; Liu, Q.; Zhang, Y. N. Highly-selective and temperature-compensated toluene sensor based on MOF-actuated optical WGM microresonator. *Sens. Actuators B: Chem.* **2025**, *423*, 136838.
[10] Bocoș-Binținan, V.; Bocoș-Binținan, P. F.; Rozsypal, T.; Beldean-Galea, M. S. Trace detection of di-isopropyl methyl phosphonate DIMP, a by-product, precursor, and simulant of sarin, using either ion mobility spectrometry or GC-MS. *Toxics* **2025**, *13*, 102.
[11] Pellejero, I.; Almazán, F.; Lafuente, M.; Urbiztondo, M. A.; Drobek, M.; Bechelany, M.; Julbe, A.; Gandía, L. M. Functionalization of 3D printed ABS filters with MOF for toxic gas removal. *J. Ind. Eng. Chem.* **2020**, *89*, 194–203.
[12] Oh, S.; Lee, S.; Lee, G.; Oh, M. Boosted ability of ZIF-8 for early-stage adsorption and degradation of chemical warfare agent simulants. *Nanoscale Adv.* **2023**, *5*, 6449–6457.
[13] Li, H. B.; Ma, L.; Zhou, L. Y.; Gao, J.; Huang, Z. H.; He, Y.; Jiang, Y. J. Magnetic integrated metal/enzymatic nanoreactor for chemical warfare agent degradation. *Colloids Surf. A: Physicochem. Eng. Aspects* **2019**, *571*, 94–100.
[14] Lafuente, M.; De Marchi, S.; Urbiztondo, M.; Pastoriza-Santos, I.; Pérez-Juste, I.; Santamaría, J.; Mallada, R.; Pina, M. Plasmonic MOF thin films with Raman internal standard for fast and ultrasensitive SERS detection of chemical warfare agents in ambient air. *ACS Sens.* **2021**, *6*, 2241–2251.
[15] Oh, S.; Lee, S.; Lee, G.; Oh, M. Enhanced adsorption capacity of ZIF-8 for chemical warfare agent simulants caused by its morphology and surface charge. *Sci. Rep.* **2023**, *13*, 12250.
[16] Matavž, A.; Verstreken, M. F. K.; Smets, J.; Tietze, M. L.; Ameloot, R. Comparison of thin-film capacitor geometries for the detection of volatile organic compounds using a ZIF-8 affinity layer. *ACS Sens.* **2023**, *8*, 3167–3173.
[17] Wang, F.; Ouyang, Y.; Zhou, P. F.; Zhang, Y.; Gao, R. J.; Eser, B. E.; Guo, Z. NIR-accelerated cascade reaction for degradation of organophosphorus compounds by Au/PTE/ZIF-8: Cooperative effect and mechanism. *Catal. Sci. Technol.* **2024**, *14*, 3424–3435.
[18] Martin-Romera, J. D.; Borrego-Marin, E.; Jabalera-Ortiz, P. J.; Carraro, F.; Falcaro, P.; Barea, E.; Carmona, F. J.; Navarro, J. A. R. Organophosphate detoxification and acetylcholinesterase reactivation triggered by zeolitic imidazolate framework structural degradation. *ACS Appl. Mater. Interfaces* **2024**, *16*, 9900–9907.
[19] Liang, J. J.; Dong, Z. T.; Xu, N.; Chen, T.; Liang, J.; Xia, M. Z.; Wang, F. H. A comprehensive review of multifunctional nanozymes for degradation and detection of organophosphorus pesticides in the environment. *Toxics* **2024**, *12*, 926.
[20] Feng, Y. Y.; Hu, P.; Wang, M.; Sun, X. B.; Pan, W.; Wang, J. P. Introducing Mn into ZIF-8 nanozyme for enhancing its catalytic activities and adding specific recognizer for detection of organophosphorus pesticides. *Microchim. Acta* **2023**, *190*, 437.
[21] Huang, X. Y.; Gong, Z. J.; Lv, Y. Advances in metal-organic frameworks-based gas sensors for hazardous substances. *TrAC Trends Anal. Chem.* **2022**, *153*, 116644.
[22] Wang, Y. R.; Wang, Z. L.; Gao, Y. F.; Yan, J.; Chen, Y. L. Moisture-resistant and ppb-level trace chemical warfare agent optical gas sensor based on ZIF-67 3D photonic crystals with structural engineering. *Sens. Actuators B: Chem.* **2024**, *409*, 135602.
[23] Li, Z. H.; Liu, J. X.; Wu, H. Z.; Tang, J.; Li, Z. Y.; Xu, Y. D.; Zhou, F.; Liu, W. M. Photonic crystals constructed by isostructural metal-organic framework films. *Nano Res.* **2023**, *16*, 9569–9576.
[24] Zhou, M. J.; Hu, Y.; Qi, C. Z.; Yang, D. P.; Huang, S. M. Metal-organic framework photonic crystals with bidisperse particles-based brilliant structural colors and high optical transparency for elaborate anti-counterfeiting. *J. Colloid Interface Sci.* **2024**, *662*, 774–785.
[25] Liu, C.; Tong, Y. L.; Yu, X. Q.; Shen, H. X.; Zhu, Z. J.; Li, Q.; Chen, S. MOF-based photonic crystal film toward separation of organic dyes. *ACS Appl. Mater. Interfaces* **2020**, *12*, 2816–2825.
[26] Zhang, T. Y.; Teng, D.; Zhang, J. J.; Meng, Z. H.; Qiu, L. L. ZIF-8-CdS photonic crystal beads for slow photon effect induced enhanced photocatalysts. *Appl. Surf. Sci.* **2025**, *681*, 161461.
[27] Zhan, K.; Zhu, Y. B.; Yan, J.; Chen, Y. L. Enhanced-performance relative humidity sensor based on MOF-801 photonic crystals. *Phys. Lett. A* **2020**, *384*, 126678.
[28] Li, M. L.; Yang, W. T.; Che, G.; Gao, Y.; Zhang, C. W.; Zhou, Q.; Li, J. Y.; Pan, Q. H. Dye-encapsulated lanthanide metal-organic framework-based photonic crystals for multilevel optical anticounterfeiting application. *ACS Appl. Opt. Mater.* **2023**, *1*, 306–313.
[29] Avci, C.; Imaz, I.; Carné-Sánchez, A.; Pariente, J. A.; Tasios, N.; Pérez-Carvajal, J.; Alonso, M. I.; Blanco, A.; Dijkstra, M.; López, C. et al. Self-assembly of polyhedral metal-organic framework particles into three-dimensional ordered superstructures. *Nat. Chem.* **2018**, *10*, 78–84.
[30] Gao, Y. F.; Wang, Y. R.; Wang, Z. L.; Yan, J.; Chen, Y. L. Highly performance DMMP optical sensor based on zeolitic imidazolate frameworks three-dimensional photonic crystals. *Microchem. J.* **2024**, *199*, 110091.